

## PAPER

[View Article Online](#)  
[View Journal](#) | [View Issue](#)Cite this: *Sustainable Energy Fuels*,  
2023, 7, 4864Porous silicon-nanowire-based electrode for the  
photoelectrocatalytic production of hydrogen†Jingxian Wang,<sup>ab</sup> Caroline Keller,<sup>ac</sup> Marc Dietrich,<sup>ad</sup> Paul E. Olli,<sup>a</sup> Pascal Gentile,<sup>d</sup>  
Stéphanie Pouget,<sup>ib</sup> Hanako Okuno,<sup>e</sup> Mohamed Boutghatin,<sup>f</sup> Yan Pennec,<sup>f</sup>  
Valérie Reita,<sup>g</sup> Duc N. Nguyen,<sup>bh</sup> Hannah Johnson,<sup>i</sup> Adina Morozan,<sup>b</sup>  
Vincent Artero<sup>ib</sup>\*<sup>b</sup> and Pascale Chenevier<sup>ib</sup>\*<sup>a</sup>

Photoelectrochemical water splitting is a sustainable and environmentally friendly way to produce green hydrogen, for which the practical fabrication of low-cost photoelectrodes remains a challenge. Here we report a porous photocathode assembly based on silicon nanowires (SiNW) as a light absorber and non-precious molybdenum sulfide (MoS<sub>x</sub>) as a hydrogen-evolution catalyst. Tuning the SiNW diameter is key to select the light absorption wavelength range of the system. We demonstrate a facile and robust route to synthesize SiNWs with a controlled diameter from 13 to 48 nm directly on a porous conductive support. The high quality and homogeneity of the SiNWs grown by this method also allowed drawing unprecedented conclusions on the growth process, hinting towards a silylene path. Photocathodes bearing SiNWs covered with MoS<sub>x</sub> perform photoelectrocatalytic production of hydrogen for several hours with a faradaic yield over 98%.

Received 27th March 2023  
Accepted 13th July 2023

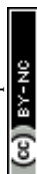
DOI: 10.1039/d3se00408b

[rsc.li/sustainable-energy](https://rsc.li/sustainable-energy)

## Introduction

Solar-driven water splitting in photoelectrochemical (PEC) cells has gained extensive attention recently to produce green hydrogen with minimal overall greenhouse gas emission.<sup>1</sup> PEC cells are based on either a single light absorber or dual light absorbers. The dual absorber system consists of a photocathode for hydrogen evolution and a photoanode for oxygen evolution. With an optimal energetic alignment of the two photoelectrodes, a sufficient overall photovoltage (>1.23 V) can be obtained to dissociate water to H<sub>2</sub> and O<sub>2</sub>.<sup>2</sup> Based on the design of polymer electrolyte membrane (PEM) electrolyzers, gas-phase PEM-PEC cells have recently emerged as a scalable design for green hydrogen production.<sup>3</sup> This device improves ion conductivity and allows the creation of higher surface area photoelectrodes.<sup>4,5</sup>

Silicon is a promising light-harvesting material for photocathode because of its low cost, and suitable band gap and valence band potential towards the hydrogen evolution reaction (HER).<sup>6</sup> Nanostructured Si, like silicon nanowires (SiNWs), attracts great interest for incorporation in PEC cell, as SiNWs have both long optical paths for efficient light absorption and short charge transport distance to the catalyst, which ensures the collection of the photogenerated charge carriers before they recombine.<sup>7–10</sup> In addition, adjusting the SiNW diameter allows to tune the band gap,<sup>11</sup> and thus the part of sun-light that will be absorbed. To date, SiNW production follows either a top-down approach, like metal assisted catalytic etching (MACE), or a bottom-up approach, like chemical vapour deposition (CVD) and solution growth.<sup>12</sup> In MACE, an HF solution dissolves bulk Si at selected area where the Si surface is not masked by metal particles, leading to the formation of SiNW arrays on planar Si<sup>9,13,14</sup> or Si powder.<sup>15</sup> This method yields SiNWs at low temperature (50 °C) but provides SiNWs only on a Si wafer substrate, and gives better results on flat surfaces.<sup>16</sup> CVD and solution growth based on Si crystallization from a silicon precursor are more versatile synthesis methods, as they allow the growth of SiNWs on different materials and support geometries.<sup>17</sup> In CVD, a gas precursor, most often SiH<sub>4</sub>, decomposes at high temperature onto metal droplets in which the Si atom dissolves, and silicon crystallization<sup>18</sup> follows at saturation. The surface of SiH<sub>4</sub>-fed CVD grown SiNWs is however a hydride Si:H surface, reactive to air and humidity, which cannot be avoided during PEC cell operation. An alternative growth process involves organosilanes<sup>19</sup> as silicon source in a vapor<sup>20,21</sup> or supercritical<sup>22</sup> phase, in which

<sup>a</sup>Univ. Grenoble Alpes, CEA, CNRS, IRIG, SyMMES, 38000 Grenoble, France. E-mail: [pascale.chenevier@cea.fr](mailto:pascale.chenevier@cea.fr)<sup>b</sup>Univ. Grenoble Alpes, CEA, CNRS, IRIG, Laboratoire de Chimie et Biologie des Métaux, 38000 Grenoble, France<sup>c</sup>Univ. Grenoble Alpes, CEA, LITEN, DEHT, 38000 Grenoble, France<sup>d</sup>Univ. Grenoble Alpes, CEA, Grenoble-INP, IRIG, PheLIQS, 38000 Grenoble, France<sup>e</sup>Univ. Grenoble Alpes, CEA, IRIG, MEM, 38000 Grenoble, France<sup>f</sup>Univ. Lille, CNRS, UMR 8520, IEMN – Institut d'Electronique de Microélectronique et de Nanotechnologie, Lille F-59000, France<sup>g</sup>Univ. Grenoble Alpes, CNRS, Institut Néel, 38000 Grenoble, France<sup>h</sup>University of Science and Technology of Hanoi, Vietnam Academy of Science and Technology, Hanoi 100000, Vietnam<sup>i</sup>Toyota Motors Europe, Materials Engineering, Hoge Wei 33, 1930 Zaventem, Belgium† Electronic supplementary information (ESI) available. See DOI: <https://doi.org/10.1039/d3se00408b>

the SiNW surface is passivated by an organic shell from the organosilane.<sup>23,24</sup>

It is known that PEC hydrogen production at Si/electrolyte interfaces has a slow kinetics,<sup>7</sup> therefore the silicon light-harvester has to be supplemented with a HER electrocatalyst. Platinum has been used extensively as catalyst in photo-electrochemical HER systems attaining up to 13% solar conversion efficiency.<sup>2</sup> However, its scarcity and high cost limit its large-scale utilization. To compensate for their lower current density, PEC cells will include membrane-electrode-assembly of larger area than electrolyzers, thus consuming a larger amount of platinum for the same production of hydrogen. In this regard, noble-metal free HER catalysts are of particular interest. Molybdenum sulfide already demonstrated high catalytic activity, nontoxicity and chemical stability.<sup>25</sup> Hu *et al.* reported that amorphous molybdenum sulfide (a-MoS<sub>x</sub>) prepared by electrodeposition from a MoS<sub>4</sub><sup>2-</sup> solution is compatible with a wide range of pH (pH = 0 to 13) with a significant geometric current density at low overpotential (15 mA cm<sup>-2</sup> at  $\eta$  = 200 mV).<sup>26</sup> Tran *et al.* pointed out that a-MoS<sub>x</sub> has a [Mo<sub>3</sub>S<sub>13</sub>]<sup>2-</sup> cluster-based polymeric structure and that eliminating terminal disulfide (S<sub>2</sub><sup>2-</sup>) ligands generates unsaturated Mo sites for H<sub>2</sub> evolution.<sup>27</sup> Recently, many methods have been developed to integrate molybdenum sulfides onto SiNWs and prepare photocathodes for H<sub>2</sub> evolution, *e.g.* electrodeposition,<sup>28</sup> photo-assisted electrodeposition,<sup>13</sup> CVD (direct<sup>29</sup> or indirect<sup>30</sup>), drop-casting,<sup>31,32</sup> spin-coating.<sup>33</sup> However, the efficient deposition of the a-MoS<sub>x</sub> catalyst on SiNWs within a porous electrode remains a challenge.

The present paper addresses the issue of building a noble-metal free, porous HER photoelectrode compatible with zero-gap PEM-PEC cells. A robust and tunable solvent-free technique is developed to grow SiNWs on a porous conductive substrate (PCS). The PEC performance of such porous photocathode is evaluated after electrodepositing a-MoS<sub>x</sub> on SiNWs as HER catalyst. A careful control of SiNW diameter from 13 to 48 nm allows maximizing the photocurrent at diameter 48 nm.

## Material and methods

### Materials

Gold(III) chloride hydrate (HAuCl<sub>4</sub>·3H<sub>2</sub>O, ~50% Au basis), sodium citrate (99%), ascorbic acid, tetraoctylammonium bromide (TOAB, 98%), sodium borohydride (NaBH<sub>4</sub>, 99%) and ammonium tetrathiomolybdate ([MoS<sub>4</sub>](NH<sub>4</sub>)<sub>2</sub>, 99.97%) were purchased from Sigma Aldrich. Dodecanethiol (98%) was purchased from Alfa Aesar. Diphenylsilane (Ph<sub>2</sub>SiH<sub>2</sub>) was purchased from Chemical Point. The porous conductive support, a carbon paper designed as a gas diffusion layer without microporous layer (Sigracet 39 AA), was purchased from FuelCellStore.

### Gold nanoparticle synthesis

Gold nanoparticles (AuNPs), as a catalyst for SiNW growth, were synthesized by different methods in order to tune their size.<sup>34</sup> The smallest AuNPs were synthesized using the Brust-Schiffrin

method.<sup>35</sup> Briefly, HAuCl<sub>4</sub>·3H<sub>2</sub>O was dissolved in water (12.5 mL, 41 mg mL<sup>-1</sup>). Toluene (120 mL) was added to the resulting solution along with TOAB (3.5 g) and dodecanethiol (0.6 mL). Then the organic phase was separated and reduced with NaBH<sub>4</sub> aqueous solution (7.5 mL, 64 mg mL<sup>-1</sup>) at room temperature for 6 hours. AuNPs of 1–3 nm were dispersed in 20 mL chloroform after evaporation of toluene and purification by ethanol. The AuNPs from 12 to 50 nm were synthesized using the Turkevich method<sup>36</sup> by mixing HAuCl<sub>4</sub>·3H<sub>2</sub>O aqueous solution with a sodium citrate solution at 100 °C for 5 minutes. The molar ratio of sodium citrate to HAuCl<sub>4</sub> (Ct/Au) was the key factor to control the particle size. By decreasing the molar ratio from Ct/Au = 5.4, to 2.3 and then to 1.4, AuNP average size increased to 12 nm, 30 nm and 40 nm. The sample was let to cool down to room temperature and stored in a dry and clean bottle at 4 °C. The AuNPs of 80 nm were grown from smaller AuNPs according to the Ziegler and Eychmüller method.<sup>37</sup> Briefly, HAuCl<sub>4</sub>·3H<sub>2</sub>O aqueous solution (60 mL, 3.3 mg mL<sup>-1</sup>) and the aqueous mixture (60 mL) of sodium citrate (4.1 mg mL<sup>-1</sup>) and ascorbic acid (2.1 mg mL<sup>-1</sup>) were slowly added to a seed solution with 12 nm AuNPs (11.5 mg L<sup>-1</sup>, 0.12 L) whilst stirring, and heated at 92 °C for 1 hour. The AuNPs in water were recovered after cooling down the solution to room temperature and stored in a dry and clean bottle at 4 °C.

### Silicon nanowire synthesis

SiNWs were grown in a 65 cm<sup>3</sup> home-built stainless-steel reactor.<sup>24</sup> AuNPs dispersed in water were transferred in an organic solvent, either toluene or ethanol, and drop-cast on a porous carbon substrate. AuNPs were drop-casted on the PCS in controlled amounts from 0.005 to 0.5 mg cm<sup>-2</sup> (the area in this paper is meant as the PCS geometric area). The AuNP-loaded PCS placed in alumina crucibles were sealed in the reactor with 6 mL diphenylsilane under vacuum and heated at 430 °C from 1 to 6 h. After cooling down to room temperature, the reactor was carefully opened and the resulting PCS-SiNW were washed with dichloromethane and acetone and dried at 80 °C. For GC-MS analysis, the sub-products were collected by washing the reactor walls with dichloromethane.

### Electrodeposition of amorphous molybdenum sulfide

a-MoS<sub>x</sub> thin films were deposited by holding PCS-SiNW at anodic potential of 0.1 or 0.2 V *versus* the normal hydrogen electrode (NHE), in a deposition bath consisting of 1.0 mM [MoS<sub>4</sub>](NH<sub>4</sub>)<sub>2</sub> in 1 M pH 7 phosphate buffer. The total density of charges was controlled at desired amount, which passed through the working electrode (1.6 cm<sup>2</sup>). After the electrodeposition of a-MoS<sub>x</sub>, the resulting PCS-SiNW-MoS<sub>x</sub> electrode was thoroughly washed with water and ethanol and dried in air at room temperature. In a control experiment, the same deposition was realized on PCS without SiNWs, yielding PCS-MoS<sub>x</sub>.

### Characterization

Scanning Electron Microscopy (SEM) (Zeiss Ultra55) was applied to characterize the nanowire morphology at an acceleration voltage of 5 kV and working distance of 5 mm. A JEOL 3010 high



resolution transmission electron microscope operated at 300 kV was used to observe AuNPs. The samples for Transmission Electron Microscopy (TEM) were prepared by the ultrasonication of AuNPs in ethanol. Both the size of AuNPs and the diameter of SiNWs were measured using ImageJ software. Scanning Transmission Electron Microscopy (STEM) measurements were performed using a Cs-corrected Titan Themis (ThermoFisher) at 200 kV. High Angle Annular Dark Field (HAADF) images were acquired with a convergence semi-angle of 20 mrad and collecting scattering from 55 mrad. Energy dispersive X-ray spectroscopy (EDX) was performed for elemental mapping using a Bruker EDX system consisting of four silicon drift detector in the Themis microscope. Electron energy loss spectroscopy (EELS) measurements were performed using a Gatan Quantum energy filter equipped with Dual EELS. For absorption spectroscopy, the SiNWs scratched with a blade from the surface of PCS-SiNW (0.25 cm<sup>2</sup>) were suspended in 2 mL dichloromethane in an ultrasound bath (10 min). The suspension was let to settle for 1 min, then the supernatant was placed in a 2 mm quartz cuvette for spectrophotometry. Powder X-ray diffraction has been carried out on a Panalytical X'Pert powder diffractometer equipped with a copper anode ( $\lambda_{K\alpha 1} = 1.5406 \text{ \AA}$ ,  $\lambda_{K\alpha 2} = 1.5444 \text{ \AA}$ ) and an X'Celerator 1D detector. It was configured in Bragg-Brentano geometry, with a variable divergence slit on the primary beam path and a set of antiscattering slits positioned before and after the sample. Axial divergence was limited by 0.02 rad Soller slits. Data analysis were performed using the Panalytical Highscore software. Raman spectra were collected on a WITec alpha 500 spectrometer, collecting the elastically scattered light (resolution  $< 0.9 \text{ cm}^{-1}$ ) filtered by an edge filter from the  $\times 100$  objective of a confocal microscope, under the excitation of a laser of wavelength 532 nm. The laser intensity was maintained at a low power of 100  $\mu\text{W}$  to avoid SiNW heating.<sup>23</sup> Gas chromatography (GC) followed by mass spectroscopy (GC-MS) analyses were performed on a PerkinElmer Clarus 580 instrument using an optima 17 column with a FID detector and a Mass Spectrometer (MS) PerkinElmer Clarus SQ8S. GC-MS analyses were performed with the following temperature program: 65 °C for 3 minutes and a ramp of 16 °C per minute until 200 °C for a total time of 20 minutes. Products were identified by comparison with the same analyses of pure compounds and with referenced MS traces from the NIST database of organic molecules. In the photoelectrochemical tests, the produced gas evolution was regularly analyzed with a PerkinElmer Clarus 580 gas chromatograph equipped with a molecular sieve 5 Å column (30 m to 0.53 mm). The gas chromatograph was set-up in the so-called point injection flow mode. Samples of 50  $\mu\text{L}$  from the headspace of the glass chamber used for the photoelectrochemical measurements, taken with a gas-tight syringe at defined times, were injected into the gas chromatograph. The area under the measured H<sub>2</sub> peaks was computed. The faradaic efficiency was calculated from the H<sub>2</sub> concentration and the calibration curves.

### Simulation of SiNW absorption spectra

The optical properties of SiNWs were numerically simulated on a model periodic line of SiNWs suspended in dichloromethane

solution in the 1.5–4.5 eV range, using the Finite Element Method (FEM, Comsol Multiphysics). We considered an incident electromagnetic plane wave generated in the dichloromethane medium and launched perpendicularly to the SiNW line (Fig. S1a and b†). The SiNWs of diameter  $d$ , separated by the period  $p$ , are cylinders, infinite along the  $z$ -direction, with periodic boundary conditions (PBC) along the  $x$ -direction, and perfect matching layers (PML) along the  $y$ -direction to absorb the outgoing waves. Diameters  $d = 13$  to 48 nm were matched with periods  $p = 60$  to 180 nm, as an optimal ratio to limit calculation time and interference between SiNWs. The reflection ( $R$ ), transmission ( $T$ ) and absorption ( $A = 1 - R - T$ ) coefficients are calculated considering the transverse electric ( $E_z$ , TE) and transverse magnetic ( $H_z$ , TM) polarizations. At the main absorbance peak, the opacity ( $1 - T$ ), corresponding to the experimentally measured absorbance, is due to both reflection (20%) and absorption (40%) of the electromagnetic wave by the SiNW (Fig. S1c†).

### Photoelectrochemical measurements

The photoelectrochemical measurements were performed in a degassed electrolyte (0.5 M H<sub>2</sub>SO<sub>4</sub>, pH 0.3) by argon bubbling, in a three-electrode configuration purpose-designed cell and using a SP-300 Bio-Logic potentiostat. The photocathodes were used as working electrode and placed in front of the light source. Ag/AgCl in 3 M KCl was used as the reference electrode and either a Pt wire (in linear scan voltammetry tests) or a Ti wire (in chronoamperometry tests) as the counter electrode, both separated from the working electrode compartment by porous glass frits. The voltages reported were calculated *versus* the reversible hydrogen electrode (RHE) according to the reference electrode calibration results before and after each test. The system was illuminated with a parallel beam from a Newport xenon lamp set at 280 W passing through an AM 1.5 filter and tuned to 100 mW cm<sup>-2</sup> to simulate closely the illumination of 1 Sun, and calibrated before each test with a silicon photodiode at the working electrode position.<sup>38</sup> The current density–potential ( $J$ – $V$ ) polarization curve was measured *via* a linear sweep voltammetry from 0.2 V to  $-0.5 \text{ V vs. RHE}$ . Current density–time ( $I$ – $t$ ) curve was measured *via* a chronoamperometry at  $-0.15 \text{ V vs. RHE}$  for at least 1 hour with N<sub>2</sub> bubbling or in a tightly closed environment after N<sub>2</sub> degas for 20 minutes. The amount of H<sub>2</sub> produced under continuous irradiation was quantified by gas chromatography analysis of the headspace after ensuring that all H<sub>2</sub> bubbles have moved up to the headspace.

## Results and discussion

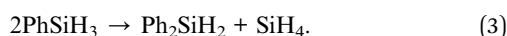
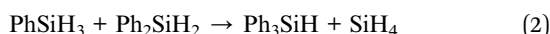
### Controlled SiNW growth: SiNW diameter and density

SiNWs were grown on a porous conductive support (PCS) following a process that we described earlier.<sup>23</sup> As PCS, we selected a gas diffusion layer developed for fuel cells, made of a macro-porous network of carbon fibers stable to SiNW growth conditions. Diphenylsilane was used as the silicon source and AuNPs as the catalyst, and the growth took place in a closed

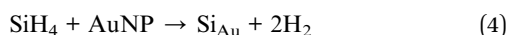


stainless steel reactor. In our previous work, we synthesized freestanding SiNWs and SiNW-grown-on-graphite composites as lithium battery anode materials,<sup>23,24,34</sup> for which a control of the average diameter was found critical.<sup>34</sup> In the present case, the use of SiNWs as light absorbers requires not only a controlled average diameter but also a narrow diameter distribution and a high quality of crystalline structure.<sup>39</sup> For this purpose, gold was chosen as the growth catalyst because it gives access to SiNW with high crystallinity and a straight morphology.<sup>18</sup> We tuned both the gold catalyst size<sup>34,40</sup> and the pressure in the reactor<sup>18,41</sup> as control parameters known to determine the SiNW diameter.

In the reactor, diphenylsilane  $\text{Ph}_2\text{SiH}_2$  undergoes thermal decomposition, supposedly following disproportionation towards silane  $\text{SiH}_4$  in several steps:<sup>42,43</sup>



Then silane decomposes on the catalyst particles, turning the pure Au solid into a melted eutectic Au–Si droplet when attaining the eutectic temperature 363 °C:



where  $\text{Si}_{\text{Au}}$  stands for a dissolved Si atom. When the droplet saturates in Si, crystallization occurs forming a SiNW.<sup>18,23</sup>

The first parameter we optimized is the amount of light-absorbing semiconductor, *i.e.* the SiNW areal density. It was tuned by two independent parameters: the loading of seeds (AuNPs of 1–3 nm diameter) on the porous conductive support,  $C_{\text{AuNP}}$ , and the amount of diphenylsilane in the reactor to tune the SiNW length. The SiNW areal densities are presented on Fig. 1a for 5 series of samples. We checked by SEM (Fig. S2b–g†) that the diameter of the SiNWs remained the same ( $13 \pm 2$  nm). The SiNWs obtained here show remarkably high structural

quality and uniformity. The SiNW areal density appears to increase with  $C_{\text{AuNP}}$ , and plateaus above  $0.8 \text{ mg cm}^{-2}$ . Above this limit, the SiNW coverage was not conformal. Excess SiNWs formed 10–20  $\mu\text{m}$  balls loosely bound to the PCS (Fig. S2g and h†). These SiNW balls absorb light but they are unfit to photo-electrocatalysis, because of their low electrical connexion to the current collector. The SiNW loading was thus set at the highest and most conformal SiNW coverage,  $0.8 \text{ mg cm}^{-2}$ .

Thanks to the very high quality and reproducibility of the growth process in these conditions, we could infer interesting mechanistic details on the growth mechanism. The mass of SiNWs is proportional to their number, determined by the number of seeds  $C_{\text{AuNP}}$ , and to their average length, determined by the growth rate. Following eqn (4), the growth rate is proportional to the partial pressure of silane,<sup>18</sup>  $p_{\text{SiH}_4}$ . We estimate  $p_{\text{SiH}_4}$  from the global pressure  $P$  just before growth starts. Indeed, when the temperature attains 363 °C, after 10 minutes heating, the AuNP catalysts are not yet active. Diphenylsilane would turn to silane *via* the disproportionation reactions (1)–(3), for which we assume a chemical dynamics of global order  $\alpha$  in the form  $p_{\text{SiH}_4} \propto p_{\text{DPS}}^\alpha$ , where  $p_{\text{DPS}}$  is the partial pressure in diphenylsilane. Disproportionation is slow at low temperature<sup>42</sup> so that the gas phase consists mainly in diphenylsilane, and the total pressure  $P_{363^\circ\text{C}}$  is close to  $p_{\text{DPS}}$ . Thus,  $p_{\text{SiH}_4}$  at the start of growth would scale as:  $p_{\text{SiH}_4} \propto (P_{363^\circ\text{C}})^\alpha$ , where  $\alpha$  is expected in the range 3–4, depending on the relative rates of reactions (1)–(3). We plot the SiNW areal density *vs.*  $C_{\text{AuNP}} \times (P_{363^\circ\text{C}})^\alpha$  for all growth conditions with various values of  $\alpha$ . The 5 series gather onto a common line only for  $\alpha = 1$  (Fig. 1b), showing that the reaction is of apparent first order. A first order dynamics is a very surprising result in view of the disproportionation mechanism, which involves second order steps (1)–(3).

Alternatively, organosilanes can undergo homolytic decomposition,<sup>44–47</sup> a first order reaction yielding highly reactive silylenes. Thermal homolysis into silylene was mainly reported at higher temperature (above 600 °C), but the high substitution of  $\text{Ph}_2\text{Si}$  could considerably stabilize the di-radical, as for the

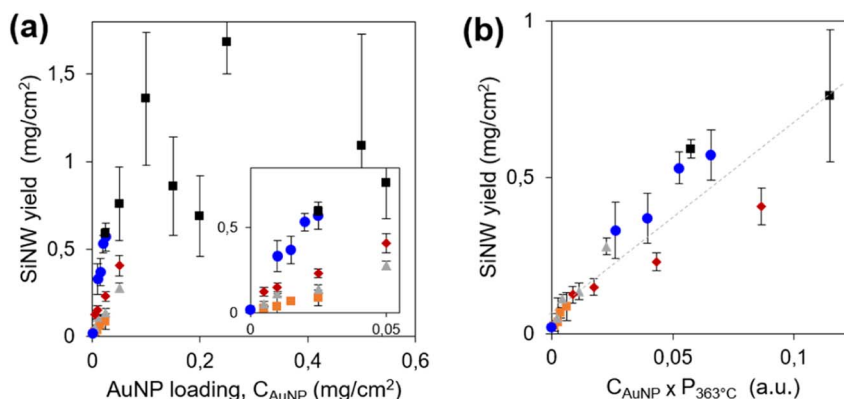
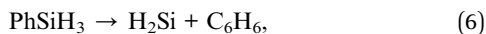
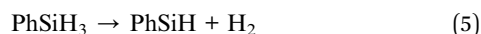


**Fig. 1** Silicon nanowire yield, expressed as the areal concentration in silicon, as a function of the gold seed loading,  $C_{\text{AuNP}}$ , (a) and as a function of  $C_{\text{AuNP}} \times P_{363^\circ\text{C}}$  where  $P_{363^\circ\text{C}}$  is the pressure at 363 °C in the reactor (b). Seeds were 1–3 nm AuNPs. Diphenylsilane loading in the reactor: 1 mL (yellow squares), 4 mL (gray triangles, red diamonds), 6 mL (blue circles, black squares). The dotted line is the best linear correlation for all samples with  $C_{\text{AuNP}} < 0.12 \text{ mg cm}^{-2}$  ( $R^2 = 0.91$ ).

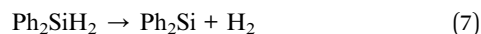




trityl radical, and thus lower the energy barrier. Additionally, the high pressure in our reactor will increase the rate of homolysis, as previously reported.<sup>48</sup> Homolytic decomposition of phenylsilane was reported<sup>44,48</sup> to follow two simultaneous paths:



among which the formation of the most substituted silylene (5) is 7 times more frequent. We can thus assume that diphenylsilane would decompose preferentially into diphenylsilylene  $\text{Ph}_2\text{Si}$  and in a lesser extent phenylsilylene  $\text{PhSiH}$ , yielding hydrogen and benzene as by-products along reactions:



Indeed, analysis of the by-products of SiNW growth by GC-MS (Fig. S3†) showed the formation of hydrogen, as expected, and of benzene, the presence of which is not explained by the disproportionation mechanism. Benzene is detected at a low but constant yield, showing that reaction (8) represents about 5% of diphenylsilane decomposition. If the relative frequencies of paths (7) and (8) follow the tendency measured for phenylsilane homolytic paths (5) and (6), it would mean that about 40% of diphenylsilane decomposes by thermal homolysis. Thus, based on our chemical dynamics data and by-product analysis, we propose for SiNW growth from diphenylsilane a mechanism involving homolytic cleavage following reactions (7) and (8) even at the surprisingly low temperature of 430 °C, in addition to the usually cited<sup>23,43,49</sup> disproportionation reaction.

As a second parameter, we optimized the SiNW diameter to shift their light absorption in the visible range. The SiNW diameter is known to depend on the AuNP catalyst size in CVD processes.<sup>34,40</sup> Using three synthesis methods, we synthesized AuNP colloids within a wide range of sizes, with a narrow size

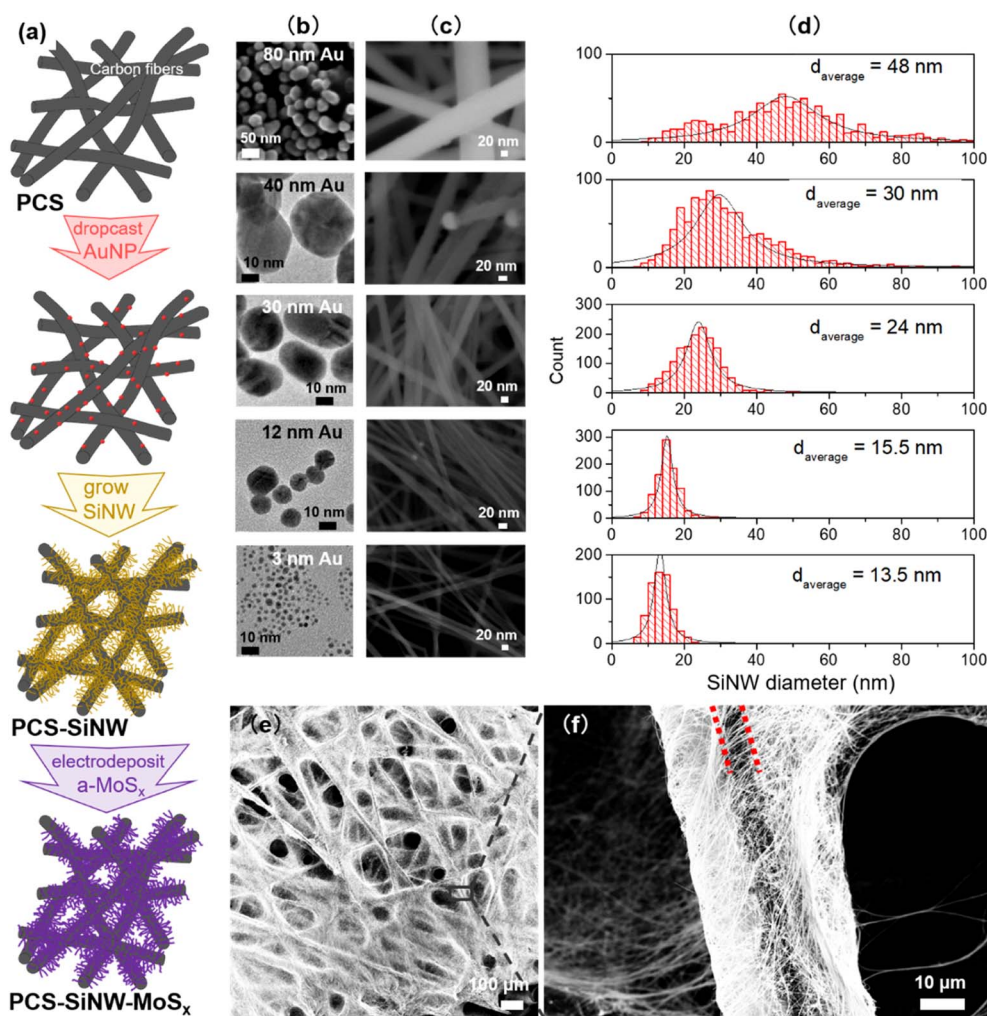


Fig. 2 Tuning SiNW diameter by the size of AuNPs: (a) scheme of the PCS-SiNW-MoS<sub>x</sub> photocathode fabrication. SEM and TEM images of the AuNPs of size 3–80 nm (b) and the subsequent SiNWs grown from them (c); (d) corresponding SiNW diameter histograms (>500 counts); SEM images of the PCS-SiNW (e) and close up view of a single carbon fiber (f). Red dotted lines highlight the diameter of the carbon fiber.



distribution (Fig. 2b). Small AuNPs (3 nm) were synthesized with dodecanethiol stabilization in an organic solvent while bigger AuNPs (12–80 nm) were made in water with citrate stabilization. AuNP solutions were drop cast on the PCS and submitted to SiNW growth. SiNWs of increasing diameters (Fig. 2c and d) grew from all seeds. The PCS-SiNW are homogeneously covered with straight SiNWs, while the samples remain porous (Fig. 2e and f). The SiNW diameter does not increase linearly with the AuNP size. Indeed, the silane pressure in the reactor is a second stringent condition determining the SiNW diameter.<sup>18,34</sup> Here the reactor loading, and thus the silane pressure profile during the growth, was set to a medium value, limiting the growth of SiNWs larger than 50 nm, but allowing higher growth rates.

The diameter of the SiNWs determines their absorption wavelength.<sup>50</sup> Accordingly, from SiNWs of diameter 13 to 42 nm, PCS-SiNW shifted from a dark bluish to yellowish colour (Fig. 3a), and the absorption spectra of SiNWs, scratched from PCS-SiNW and suspended in dichloromethane, show a progressive blue shift of the plasmon resonance<sup>51</sup> band as the SiNW diameter increases (Fig. 3b). Spectrophotometry could however not distinguish light absorption, useful for photoelectrocatalysis, from light diffusion or reflection by the SiNWs. The light absorption of SiNWs was thus simulated numerically

using the Finite Element Method (FEM, Comsol Multiphysics) (Fig. S1†), as we previously reported.<sup>50</sup> The opacity, corresponding to the non-transmitted light as in the absorbance measurement, was calculated for diameters fitting the experimental SiNW sizes (Fig. 3c). The simulated spectra reproduce well the double-shoulder shape of SiNW absorbance, and the shift of the plasmonic peak position with diameter (Fig. 3d). Additionally, the simulated wave (Fig. S1c†) shows that, at the main absorbance peak, the opacity is due to both reflection (20%) and absorption (40%) of the electromagnetic wave by the SiNW. This confirms the relevance of SiNWs as photosensitizers with a tunable absorption range. PCS-SiNW with SiNW diameter 48 nm, harvesting a larger part in the visible range, was selected for photoelectrocatalysis.

### MoS<sub>x</sub> electrodeposition and sample characterization

a-MoS<sub>x</sub> was deposited on SiNWs by electrodeposition immediately after nanowire growth. The total charge density that passed through the working electrode ( $\Delta Q$ ) was varied from 0 to 50 mC cm<sup>-2</sup> to tune the a-MoS<sub>x</sub> amount.<sup>27</sup> The as-grown 48 nm-SiNWs have a smooth surface (Fig. 4a) which becomes rough after electrodeposition (Fig. 4b). STEM-HAADF imaging shows that a-MoS<sub>x</sub> forms a shell around the SiNWs (Fig. 4c). Coverage

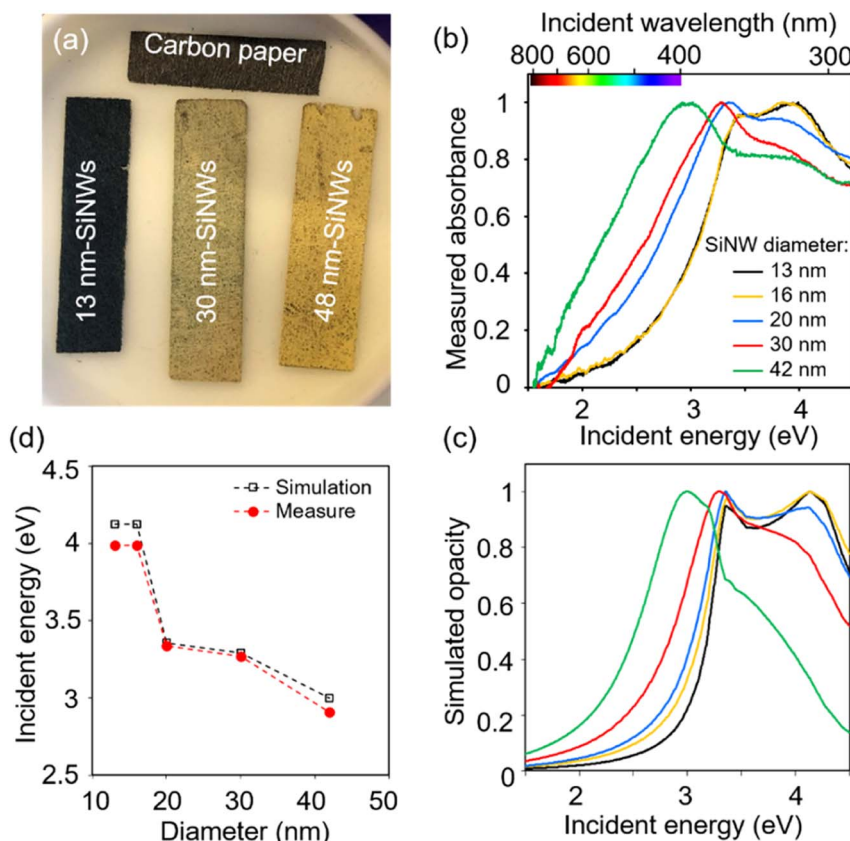


**Fig. 3** Tuning SiNW absorption wavelength by their diameter: (a) photograph of PCS-SiNW. (b) Normalized spectra of measured absorbance for SiNWs from PCS-SiNW with 13, 16, 20, 30 and 42 nm SiNWs. The rainbow indicates the visible range. (c) Normalized spectra of simulated opacity for TE polarization of SiNWs of diameters 13 to 42 nm (same legend as (b)). (d) Position of the plasmonic peak as a function of the SiNW diameter in measured and simulated spectra.



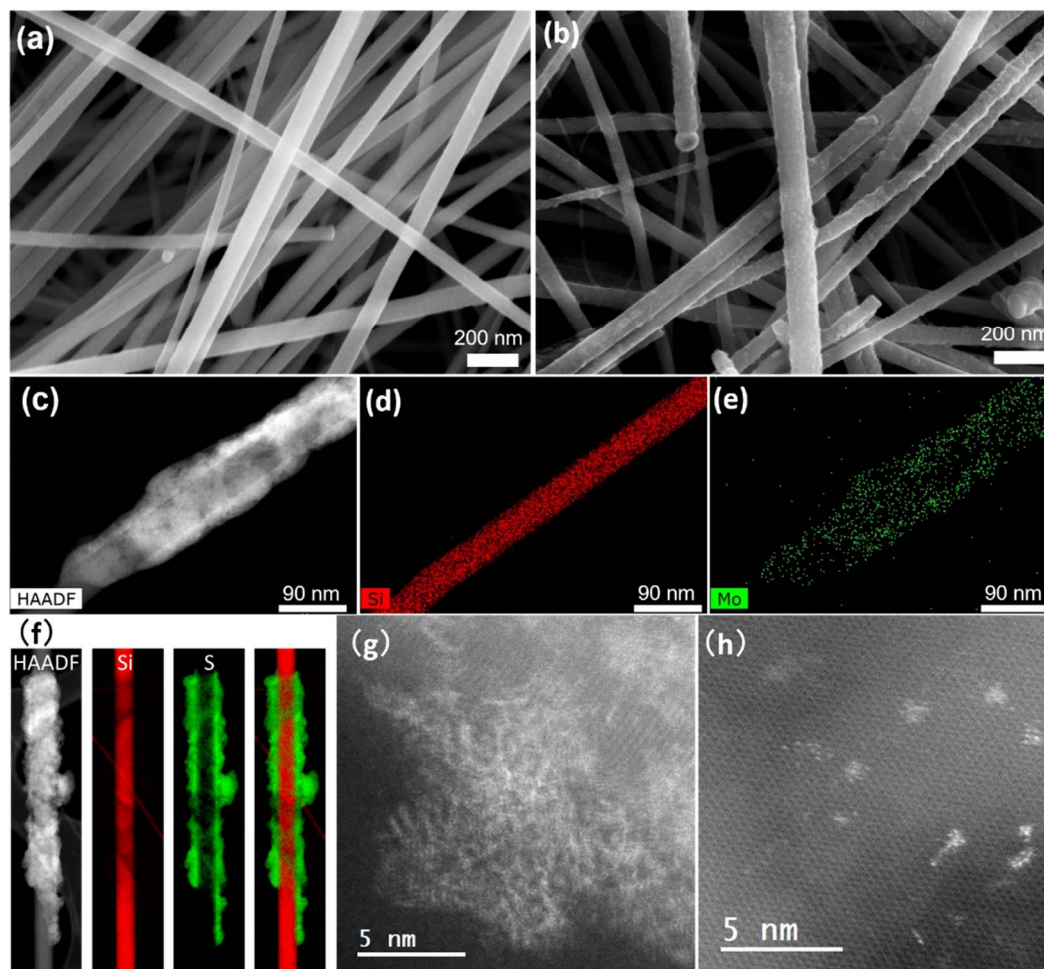


Fig. 4 SEM images of (a) 48 nm-SiNWs, (b) SiNW-MoS<sub>x</sub> with  $\Delta Q = 6 \text{ mC cm}^{-2}$  (c) HAADF-STEM image of SiNW-MoS<sub>x</sub> and EDX mapping profile of (d) Si(K<sub>α</sub>) and (e) Mo(K<sub>α</sub>); (f) STEM-HAADF image and EELS mapping profile of element Si (L edge at 99 eV) and S (L edge at 165 eV); (g, h) High-resolution HAADF-STEM images of a-MoS<sub>x</sub>.

is partly inhomogeneous. EDX (Fig. 4d and e) and EELS (Fig. 4f) confirmed that this layer is composed of Mo and S. The a-MoS<sub>x</sub> layer can be made thicker by raising the charge passed on SiNWs and reaches several tens of nanometers (Fig. S4†).

TEM was used to study the structure of SiNWs and SiNW-MoS<sub>x</sub>. The as-grown SiNWs present a crystalline silicon core surrounded by an amorphous shell of 1–2 nm (Fig. S5a and b†), which is composed of phenyl moieties<sup>23</sup> and a very low degree of oxygen characterized by XPS in our previous work.<sup>24</sup> The high-resolution TEM imaging was employed to reveal MoS<sub>x</sub> atomic structure deposited on this layer. However, conventional TEM would not tell apart the atomic arrangement of MoS<sub>x</sub> (Fig. S5d†) from the amorphous shell surrounding the SiNWs. With the more sensitive HAADF-STEM technique, images show brighter spots that can be interpreted as Mo atoms on the Si lattice (Fig. 4g and h). Agglomerated a-MoS<sub>x</sub> particles without well-defined lattice appear in contrast to the silicon core, while fringes present in small regions indicate an amorphous structure with some short-range order (Fig. 4g). The separated nano-sized a-MoS<sub>x</sub> particles and sub-nano-sized clusters (Fig. 4h) are reminiscent of the a-MoS<sub>x</sub> structure reported by Tran *et al.*<sup>27</sup>

According to their work, a-MoS<sub>x</sub> particles consist of [Mo<sub>3</sub>] clusters, in either one-dimensional chains or two-dimensional networks. Here it seems that these particles can scatter over the nanowire surface as in Fig. 4h or agglomerate in a short-range order as in Fig. 4g.

We employed Raman spectroscopy and X-ray diffraction (Fig. 5) to determine the structure of the molybdenum sulfide in PCS-SiNW-MoS<sub>x</sub>. As the signal from the thin a-MoS<sub>x</sub> catalytic layer could not be resolved from the signals of PCS and SiNWs, the amount of deposited a-MoS<sub>x</sub> was increased 100 times for this analysis. Beside the characteristic peak of silicon at 520 cm<sup>-1</sup>, the Raman spectrum of PCS-SiNW-MoS<sub>x</sub> (Fig. 5a) shows the full pattern of a-MoS<sub>x</sub>,<sup>27</sup> including S-S vibration bands  $\nu(\text{S-S})_t$  and  $\nu(\text{S-S})_{br/sh}$  at 510 and 550 cm<sup>-1</sup>, a bridging  $\nu(\text{Mo}_3-\mu\text{S})$  band at 450 cm<sup>-1</sup> and  $\nu(\text{Mo-S})$  vibration bands at 320, 350 and 370 cm<sup>-1</sup>.

The X-ray diffractogram of PCS-SiNW-MoS<sub>x</sub> presents the same peaks as the control PCS-SiNW (Fig. 5b), mainly attributed to graphitic carbon from the PCS and crystalline gold and silicon from the SiNWs, except for a wide band at  $2\theta = 16\text{--}19^\circ$  (Fig. 5b inset). The expected peaks from crystalline MoS<sub>2</sub> are not





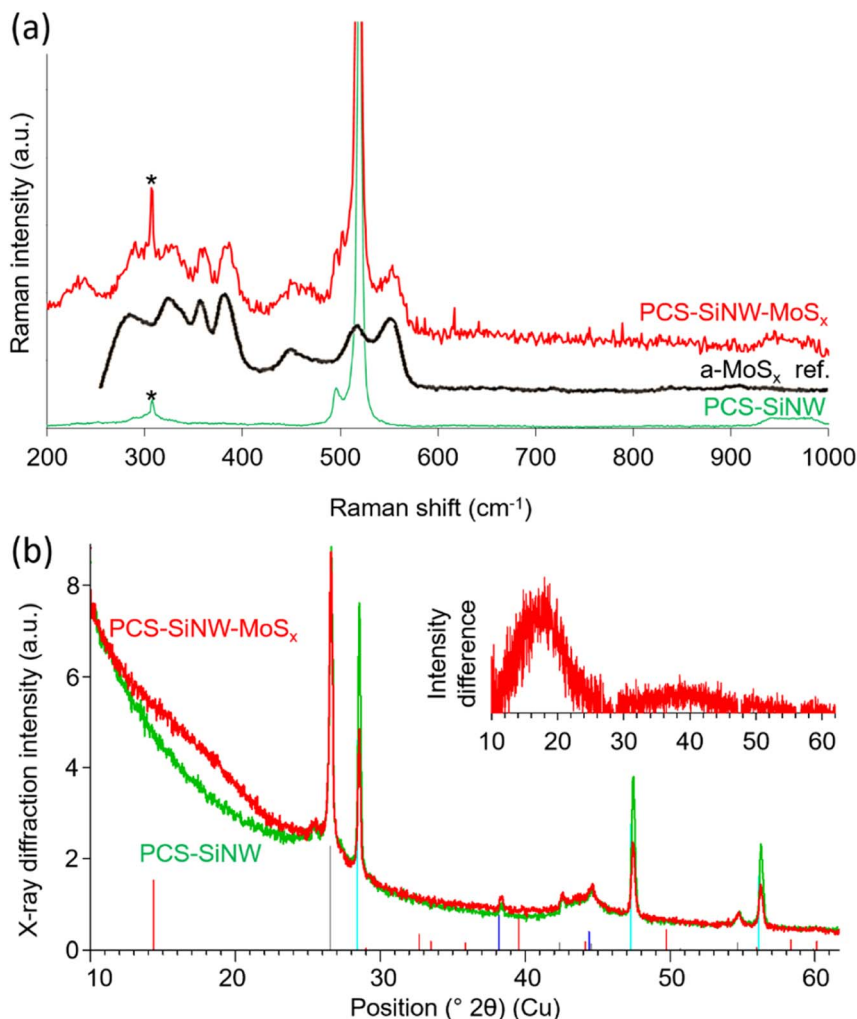


**Fig. 5** Characterization of electrodeposited a-MoS<sub>x</sub>: (a) Raman spectra and (b) X-ray diffractograms of PCS-SiNW (green) and PCS-SiNW-MoS<sub>x</sub> (red). The black line in (a) shows the reference Raman spectrum of a-MoS<sub>x</sub> (from ref. 27). As collection time was long (10–60 minutes), a known artefact arising from the Raman optics appears on the spectra at 307 cm<sup>-1</sup> (labeled as \*). Vertical lines in (b) show the reference patterns for graphitic carbon (grey), silicon (cyan), gold (blue) and crystalline MoS<sub>2</sub> (red). (b) Inset: X-ray diffraction intensity difference obtained by subtracting the PCS-SiNW from the PCS-SiNW-MoS<sub>x</sub> diffractogram.

observed. We checked by recording diffractograms both in transmission and reflection that the pattern was the same, showing that the missing MoS<sub>2</sub> peaks did not depend on sample orientation. The broad 16–19° band (Fig. 5b inset) indicates a purely amorphous structure with a nearest neighbor distance of 0.26 nm, slightly higher than that of crystalline MoS<sub>2</sub> (ref. 52) (0.25 nm) and consistent with Mo–S bond lengths reported for reference a-MoS<sub>x</sub> catalyst.<sup>53</sup>

### PEC performance of SiNW-MoS<sub>x</sub>

Photoelectrocatalytic (PEC) performance were measured in 0.5 M H<sub>2</sub>SO<sub>4</sub> under chopped illumination of simulated AM 1.5G sunlight (100 mW cm<sup>-2</sup>) using a three-electrode configuration. Illuminating PCS-SiNW resulted in a slight positive shift of the open circuit potential, indicating a p-type conductivity that is usually observed in undoped SiNWs.<sup>54,55</sup> The current–voltage (*J*–*V*) curve of PCS-SiNW-MoS<sub>x</sub> under chopped illumination was

compared with that of PCS-SiNW and PCS-MoS<sub>x</sub> as controls (Fig. 6a). On one hand, PCS-MoS<sub>x</sub> shows a high electrocatalytic activity but no photocurrent. On the other hand, PCS-SiNW produces a very low photocurrent (0.02 mA cm<sup>-2</sup> at –0.4 V *vs.* RHE) with an onset at –0.15 V *vs.* RHE. The PCS-SiNW-MoS<sub>x</sub> photocathode ( $\Delta Q = 6$  mC cm<sup>-2</sup> for a-MoS<sub>x</sub> electrodeposition) exhibits a much higher photocurrent of 0.23 mA cm<sup>-2</sup> at –0.15 V *vs.* RHE and an anodic shift of the onset potential by 0.1 V, demonstrating that a-MoS<sub>x</sub> catalyst accelerates the electron transport significantly from undoped SiNWs to the electrolyte to convert protons into H<sub>2</sub>. In general, we observed that the dark current for H<sub>2</sub> evolution for PCS-SiNW-MoS<sub>x</sub> cathode is cathodically shifted with regards to the PCS-MoS<sub>x</sub> control, highlighting the intrinsic resistance of the undoped SiNWs.

A thin passivation layer surrounding the SiNWs proved necessary in producing a PEC photocurrent from silicon-based photocathodes.<sup>56,57</sup> Here, the passivation is provided by the native organic shell of phenyls, brought by the diphenylsilane





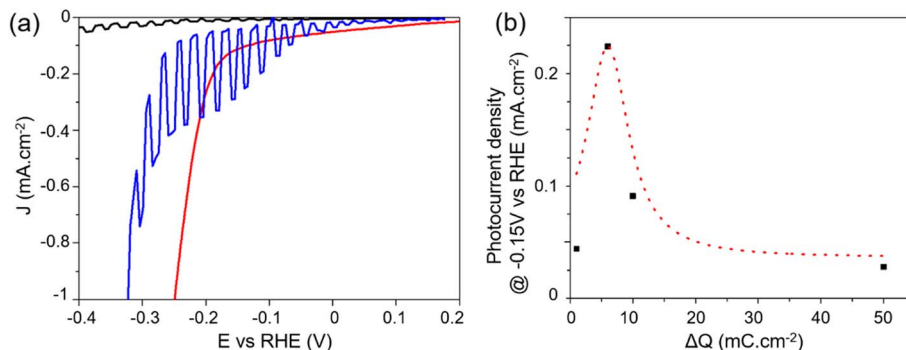


Fig. 6 Photoelectrocatalysis performance of PCS-SiNW-MoS<sub>x</sub> with 48 nm-SiNWs: (a) *J*-*V* curves of PCS-SiNW-MoS<sub>x</sub> (blue), PCS-SiNW (black) and PCS-MoS<sub>x</sub> (red) electrodes in 0.5 M H<sub>2</sub>SO<sub>4</sub> electrolyte under chopped illumination (a-MoS<sub>x</sub> deposition:  $\Delta Q = 6 \text{ mC cm}^{-2}$ ). (b) Photocurrent density of PCS-SiNW-MoS<sub>x</sub> at  $-0.15 \text{ V vs. RHE}$  as a function of  $\Delta Q$  during a-MoS<sub>x</sub> electrodeposition (*J*-*V* curves in Fig. S5†). The Gaussian dotted line is a guide to the eye.

reagents during growth, able to slow down Si oxidation.<sup>24,58</sup> We observed a 17% degraded PEC performance (Fig. S6a†) when delaying the a-MoS<sub>x</sub> deposition 2 weeks after SiNW growth, which lets a limited oxidation happen on the SiNW surface. More, etching the SiNW surface by dissolution in an HF solution before a-MoS<sub>x</sub> deposition resulted in a complete loss of PEC performance. As a further check, we prepared PCS-SiNW-MoS<sub>x</sub> electrodes devoid of hydrophobic shell using a conventional SiNW CVD growth method<sup>59</sup> fed with SiH<sub>4</sub>. In this process, the native Si:H surface on SiNWs rapidly turns to oxide once in contact with air. The CVD growth parameters were first optimized to fit the SiNW diameter and areal density with the best PCS-SiNW-MoS<sub>x</sub> electrodes produced in this study. Then MoS<sub>x</sub> was deposited on the obtained PCS-SiNW, but no photocurrent was recorded from these samples (Fig. S6b†). Let us note that a much larger current was recorded during the a-MoS<sub>x</sub> electrodeposition step, probably due to silicon oxidation. These data indicate that an as low as possible SiO<sub>2</sub> layer and the presence of a protective shell on the SiNWs play a vital role in the stability of the silicon-catalyst interface.

As expected, comparing PCS-SiNW-MoS<sub>x</sub> photocathodes with 13 nm- and 48 nm-SiNWs (Fig. S7†) proved that the largest SiNWs provide a 5-fold higher photocurrent than the smaller

(0.25 vs. 0.05 mA cm<sup>-2</sup> at  $-0.15 \text{ V vs. RHE}$ ) while the photocurrent onset is similar ( $-0.05 \text{ V vs. RHE}$ ). The optimal areal density of silicon was found similar for all SiNW diameter tested (Fig. S8†). The PEC activity of PCS-SiNW-MoS<sub>x</sub> photocathode depends much more strongly on the amount of a-MoS<sub>x</sub> deposited on SiNWs, following a volcano-shaped curve (Fig. 6b). The a-MoS<sub>x</sub> loading at the optimum  $\Delta Q = 6 \text{ mC cm}^{-2}$  is 31 nmol cm<sup>-2</sup> assuming a 2e<sup>-</sup> oxidation process from [MoS<sub>4</sub>]<sup>2-</sup> precursor to a-MoS<sub>x</sub>. As seen by electron microscopy, this optimal layer consists of an inhomogeneous layer shelling partially the SiNWs. A full coverage of the SiNWs by a-MoS<sub>x</sub> is obtained at higher loading (Fig. S4d†), but the PEC performance drops, maybe due to a lack of conductivity within thick a-MoS<sub>x</sub> layers.

The stability of the PCS-SiNW-MoS<sub>x</sub> photocathode was examined by chronoamperometry analysis at  $-0.15 \text{ V vs. RHE}$  (Fig. 7a and S9b†). The photocurrent dropped by 25–50% after 1 hour, depending on the sample. Gas chromatography analysis of the cell headspace allowed to determine a faradaic yield  $98 \pm 5\%$  for hydrogen production after 1 hour (Fig. S9†). SEM images of the sample before and after chronoamperometry (Fig. 7b and c) show a change in morphology of the MoS<sub>x</sub> film: initially wrapping individual SiNWs, the film bundles up substantially

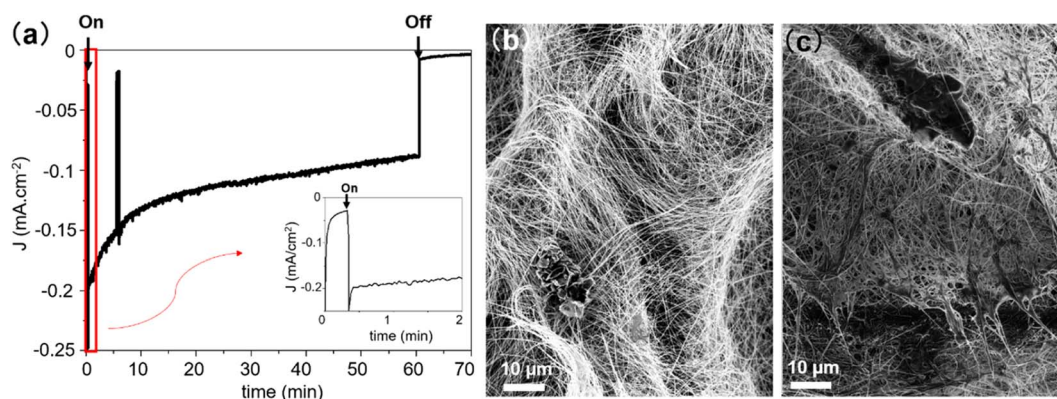


Fig. 7 (a) Chronoamperometry of PCS-SiNW-MoS<sub>x</sub> at  $-0.15 \text{ V vs. RHE}$  in 0.5 M H<sub>2</sub>SO<sub>4</sub> under illumination (48 nm-SiNWs,  $\Delta Q_{\text{MoS}_x} = 6 \text{ mC cm}^{-2}$ ) with N<sub>2</sub> bubbling. SEM images of the electrode before (b) and after (c) the stability test.



the nearby SiNWs after PEC. Detachment and re-aggregation of small a-MoS<sub>x</sub> nanoparticles was often observed in a-MoS<sub>x</sub> film as HER catalyst in acid.<sup>60,61</sup> This film could clog the electrode porosity and prevent electrolyte access to the internal part. Long-term oxidation of SiNWs by water during PEC could be another reason for the drop in photocurrent.

## Conclusion

In summary, a facile route has been proposed to develop operational porous photocathodes based on SiNWs as light absorbers and MoS<sub>x</sub> as the HER catalyst. SiNWs were grown in direct contact with the carbon porous conductive support *via* a low-cost and tunable chemical method, applicable to other porous substrates with various morphology. Our well-controlled growth process allowed optimizing the efficiency of SiNW light absorption by fine-tuning their diameter and thus their absorption spectrum. It also provides a native hydrophobic passivation layer on silicon preventing oxidation, which appears essential in photoelectrocatalysis, probably by ensuring a low-barrier electrical contact between light absorber and catalyst. As compared to other non-noble metal photocatalytic systems on undoped silicon,<sup>62</sup> the PCS-SiNW-MoS<sub>x</sub> photocathode exhibits an interesting photocurrent of 0.23 mA cm<sup>-2</sup> at -0.15 V *vs.* RHE. Further work will focus on doping the SiNWs<sup>13</sup> and the a-MoS<sub>x</sub> catalyst<sup>63</sup> to maximize the anodic shift of the onset potential, and design new growth seeds to investigate SiNWs with diameters in the 50–100 nm range. As the hydrophobic protective layer natively grown on the SiNWs proved to prevent oxidation in air and water, we will improve the durability of this shell by enhancing its passivating efficiency, as reported for bulk silicon photocathodes.<sup>58</sup> Finally, this work provides a new scalable approach to develop porous photocathode based on easily tunable silicon nanostructures and noble-metal-free HER catalyst.

## Author contributions

J. W. prepared the samples and wrote the first manuscript. J. W., P. E. O. and C. K. grew the AuNPs of varied sizes. J. W. and H. O. performed the electron microscopy. J. W., P. E. O. and A. M. performed the photoelectrochemical tests. D. N. N. designed the photoelectrochemical tests. M. D. and P. G. designed and realized the CVD growth of the SiNW samples without phenyl protective layer. S. P. designed and performed the XRD characterization. P. C. measured the absorption spectra and wrote the manuscript. V. R. designed and performed the Raman characterization. M. B. and Y. P. designed and realized the finite element simulation of light absorption. H. J., A. M., V. A. and P. C. conceived and designed the experiments, and ensured supervision and funding. All authors discussed the results and commented on the manuscript.

## Conflicts of interest

There are no conflicts to declare.

## Acknowledgements

J. W. and P. E. O. acknowledge the financial support from European Horizon 2020's Project Sun-to-X under agreement no. 883264. This work was supported by the Agence Nationale de la Recherche (Labex ARCANÉ, CBH-EUR-GS, ANR-17-EURE-0003). M. B. and Y. P. acknowledges the financial support from the project PRCE-ANR-POCOMA under agreement ref. ANR-21-CE09-0040-01. The authors thank Adeline Jorge-Robin and Jennifer Fize for GC-MS and GC quantitative analyses.

## References

- 1 G. Segev, C. Hahn, Z. J. Xu, W.-H. Cheng, T. G. Deutsch, C. Xiang, J. Z. Zhang, L. Hammarström, D. G. Nocera, A. Z. Weber, P. Agbo, T. Hisatomi, F. E. Osterloh, K. Domen, F. F. Abdi, S. Haussener, D. J. Miller, S. Ardo, P. C. McIntyre, T. Hannappel, S. Hu, H. Atwater, J. M. Gregoire, M. Z. Ertem, I. D. Sharp, K.-S. Choi, J. S. Lee, O. Ishitani, J. W. Ager, R. R. Prabhakar, A. T. Bell, S. W. Boettcher, K. Vincent, K. Takanabe, V. Artero, R. Napier, B. R. Cuenya, M. T. M. Koper, R. V. D. Krol and F. Houle, The 2022 Solar Fuels Roadmap, *J. Phys. D: Appl. Phys.*, 2022, **55**(32), 323003, DOI: [10.1088/1361-6463/ac6f97](https://doi.org/10.1088/1361-6463/ac6f97).
- 2 M. G. Walter, E. L. Warren, J. R. McKone, S. W. Boettcher, Q. Mi, E. A. Santori and N. S. Lewis, Solar Water Splitting Cells, *Chem. Rev.*, 2010, **110**(11), 6446–6473, DOI: [10.1021/cr1002326](https://doi.org/10.1021/cr1002326).
- 3 M. Caretti, E. Mensi, R.-A. Kessler, L. Lazouni, B. Goldman, L. Carbone, S. Nussbaum, R. A. Wells, H. Johnson, E. Rideau, J. Yum and K. Sivula, Transparent Porous Conductive Substrates for Gas-Phase Photoelectrochemical Hydrogen Production, *Adv. Mater.*, 2020, **32**, 200740, DOI: [10.1002/adma.20200740](https://doi.org/10.1002/adma.20200740).
- 4 G. Zafeiropoulos, H. Johnson, S. Kinge, M. C. M. van de Sanden and M. N. Tsampas, Solar Hydrogen Generation from Ambient Humidity Using Functionalized Porous Photoanodes, *ACS Appl. Mater. Interfaces*, 2019, **11**(44), 41267–41280, DOI: [10.1021/acsami.9b12236](https://doi.org/10.1021/acsami.9b12236).
- 5 J. Rongé, S. Deng, S. Pulinthanathu Sree, T. Bosserez, S. W. Verbruggen, N. Kumar Singh, J. Dendooven, M. B. J. Roelofs, F. Taulelle, M. De Volder, C. Detavernier and J. A. Martens, Air-Based Photoelectrochemical Cell Capturing Water Molecules from Ambient Air for Hydrogen Production, *RSC Adv.*, 2014, **4**(55), 29286–29290, DOI: [10.1039/C4RA05371K](https://doi.org/10.1039/C4RA05371K).
- 6 L. Wei, R. Li, Q. Fan, C. Yu and P. Tan, Fabrication of P-Type Silicon Nanowire Array Based Photoelectrodes for the Efficient Photoelectrocatalytic Reduction of CO<sub>2</sub> to Fuels and Chemicals, *Sustain. Energy Fuels*, 2022, **6**(8), 1854–1865, DOI: [10.1039/D2SE00105E](https://doi.org/10.1039/D2SE00105E).
- 7 S. W. Boettcher, J. M. Spurgeon, M. C. Putnam, E. L. Warren, D. B. Turner-Evans, M. D. Kelzenberg, J. R. Maiolo, H. A. Atwater and N. S. Lewis, Energy-Conversion Properties of Vapor-Liquid-Solid-Grown Silicon Wire-Array Photocathodes, *Science*, 2010, **327**(5962), 185–187.



- 8 A. P. Goodey, S. M. Eichfeld, K.-K. Lew, J. M. Redwing and T. E. Mallouk, Silicon Nanowire Array Photoelectrochemical Cells, *J. Am. Chem. Soc.*, 2007, **129**(41), 12344–12345.
- 9 I. Oh, J. Kye and S. Hwang, Enhanced Photoelectrochemical Hydrogen Production from Silicon Nanowire Array Photocathode, *Nano Lett.*, 2012, **12**(1), 298–302.
- 10 S. Chandrasekaran, S. J. P. McInnes, T. J. MacDonald, T. Nann and N. H. Voelcker, Porous Silicon Nanoparticles as a Nanophotocathode for Photoelectrochemical Water Splitting, *RSC Adv.*, 2015, **5**(104), 85978–85982, DOI: [10.1039/c5ra12559f](https://doi.org/10.1039/c5ra12559f).
- 11 T. Xu, Y. Lambert, C. Krzeminski, B. Grandier, D. Stiévenard, G. Lévêque, A. Akjouj, Y. Pennec and B. Djafari-Rouhani, Optical Absorption of Silicon Nanowires, *J. Appl. Phys.*, 2012, **112**(3), DOI: [10.1063/1.4739708](https://doi.org/10.1063/1.4739708).
- 12 K.-Q. Peng, X. Wang, L. Li, Y. Hu and S.-T. Lee, Silicon Nanowires for Advanced Energy Conversion and Storage, *Nano Today*, 2013, **8**(1), 75–97, DOI: [10.1016/j.nantod.2012.12.009](https://doi.org/10.1016/j.nantod.2012.12.009).
- 13 P. D. Tran, S. S. Pramana, V. S. Kale, M. Nguyen, S. Y. Chiam, S. K. Batabyal, L. H. Wong, J. Barber and J. Loo, Novel Assembly of an MoS<sub>2</sub> Electrocatalyst onto a Silicon Nanowire Array Electrode to Construct a Photocathode Composed of Elements Abundant on the Earth for Hydrogen Generation, *Chem.–Eur. J.*, 2012, **18**(44), 13994–13999, DOI: [10.1002/chem.201202214](https://doi.org/10.1002/chem.201202214).
- 14 S. Chandrasekaran, T. Nann and N. H. Voelcker, Silicon Nanowire Photocathodes for Photoelectrochemical Hydrogen Production, *Nanomaterials*, 2016, **6**(8), 1–7, DOI: [10.3390/nano6080144](https://doi.org/10.3390/nano6080144).
- 15 B. M. Bang, H. Kim, H.-K. Song, J. Cho and S. Park, Scalable Approach to Multi-Dimensional Bulk Si Anodes via Metal-Assisted Chemical Etching, *Energy Environ. Sci.*, 2011, **4**(12), 5013–5019, DOI: [10.1039/C1EE02310A](https://doi.org/10.1039/C1EE02310A).
- 16 F. J. Wendisch, M. Rey, N. Vogel and G. R. Bourret, Large-Scale Synthesis of Highly Uniform Silicon Nanowire Arrays Using Metal-Assisted Chemical Etching, *Chem. Mater.*, 2020, **32**(21), 9425–9434, DOI: [10.1021/acs.chemmater.0c03593](https://doi.org/10.1021/acs.chemmater.0c03593).
- 17 S. Imtiaz, I. S. Amiinu, D. Storan, N. Kapuria, H. Geaney, T. Kennedy and K. M. Ryan, Dense Silicon Nanowire Networks Grown on a Stainless-Steel Fiber Cloth: A Flexible and Robust Anode for Lithium-Ion Batteries, *Adv. Mater.*, 2021, 2105917, DOI: [10.1002/adma.202105917](https://doi.org/10.1002/adma.202105917).
- 18 V. Schmidt, J. V. Wittemann and U. Gösele, Growth, Thermodynamics, and Electrical Properties of Silicon Nanowires, *Chem. Rev.*, 2010, **110**(1), 361–388, DOI: [10.1021/cr900141g](https://doi.org/10.1021/cr900141g).
- 19 H.-Y. Tuan and B. A. Korgel, Importance of Solvent-Mediated Phenylsilane Decomposition Kinetics for High-Yield Solution-Phase Silicon Nanowire Synthesis, *Chem. Mater.*, 2008, **20**(4), 1239–1241, DOI: [10.1021/cm7033068](https://doi.org/10.1021/cm7033068).
- 20 A. T. Heitsch, D. D. Fanfair, H.-Y. Tuan and B. A. Korgel, Solution–Liquid–Solid (SLS) Growth of Silicon Nanowires, *J. Am. Chem. Soc.*, 2008, **130**(16), 5436–5437, DOI: [10.1021/ja8011353](https://doi.org/10.1021/ja8011353).
- 21 J. C. Chan, H. Tran, J. W. Pattison and S. B. Rananavare, Facile Pyrolytic Synthesis of Silicon Nanowires, *Solid-State Electron.*, 2010, **54**(10), 1185–1191, DOI: [10.1016/j.sse.2010.05.011](https://doi.org/10.1016/j.sse.2010.05.011).
- 22 J. D. Holmes, K. P. Johnston, R. C. Doty and B. A. Korgel, Control of Thickness and Orientation of Solution-Grown Silicon Nanowires, *Science*, 2000, **287**, 1471–1473.
- 23 O. Burchak, C. Keller, G. Lapertot, M. Salaün, J. Danet, Y. Chen, N. Bendiab, B. Pépin-Donat, C. Lombard, J. Faure-Vincent, A. Vignon, D. Aradilla, P. Reiss and P. Chenevier, Scalable Chemical Synthesis of Doped Silicon Nanowires for Energy Applications, *Nanoscale*, 2019, **11**(46), 22504–22514, DOI: [10.1039/c9nr03749g](https://doi.org/10.1039/c9nr03749g).
- 24 S. Karuppiyah, C. Keller, P. Kumar, P. H. Jouneau, D. Aldakov, J. B. Ducros, G. Lapertot, P. Chenevier and C. Haon, A Scalable Silicon Nanowires-Grown-On-Graphite Composite for High-Energy Lithium Batteries, *ACS Nano*, 2020, **14**(9), 12006–12015, DOI: [10.1021/acsnano.0c05198](https://doi.org/10.1021/acsnano.0c05198).
- 25 P. C. K. Vesborg, B. Seger and I. Chorkendorff, Recent Development in Hydrogen Evolution Reaction Catalysts and Their Practical Implementation, *J. Phys. Chem. Lett.*, 2015, **6**(6), 951–957, DOI: [10.1021/acs.jpclett.5b00306](https://doi.org/10.1021/acs.jpclett.5b00306).
- 26 D. Merki, S. Fierro, H. Vrubel and X. Hu, Amorphous Molybdenum Sulfide Films as Catalysts for Electrochemical Hydrogen Production in Water, *Chem. Sci.*, 2011, **2**(7), 1262–1267, DOI: [10.1039/C1SC00117E](https://doi.org/10.1039/C1SC00117E).
- 27 P. D. Tran, T. V. Tran, M. Orio, S. Torelli, Q. D. Truong, K. Nayuki, Y. Sasaki, S. Y. Chiam, R. Yi, I. Honma, J. Barber and V. Artero, Coordination Polymer Structure and Revisited Hydrogen Evolution Catalytic Mechanism for Amorphous Molybdenum Sulfide, *Nat. Mater.*, 2016, **15**(6), 640–646, DOI: [10.1038/nmat4588](https://doi.org/10.1038/nmat4588).
- 28 G.-L. Zang, G.-P. Sheng, C. Shi, Y.-K. Wang, W.-W. Li and H.-Q. Yu, A Bio-Photoelectrochemical Cell with a MoS<sub>3</sub>-Modified Silicon Nanowire Photocathode for Hydrogen and Electricity Production, *Energy Environ. Sci.*, 2014, **7**(9), 3033–3039, DOI: [10.1039/C4EE00654B](https://doi.org/10.1039/C4EE00654B).
- 29 D. Hu, J. Xiang, Q. Zhou, S. Su, Z. Zhang, X. Wang, M. Jin, L. Nian, R. Nözel, G. Zhou, Z. Zhang and J. Liu, One-Step Chemical Vapor Deposition of MoS<sub>2</sub> Nanosheets on SiNWs as Photocathodes for Efficient and Stable Solar-Driven Hydrogen Production, *Nanoscale*, 2018, **10**(7), 3518–3525, DOI: [10.1039/C7NR09235K](https://doi.org/10.1039/C7NR09235K).
- 30 G. Paulraj, P. S. Venkatesh, P. Dharmaraj, S. Gopalakrishnan and K. Jeganathan, Stable and Highly Efficient MoS<sub>2</sub>/Si NWs Hybrid Heterostructure for Photoelectrocatalytic Hydrogen Evolution Reaction, *Int. J. Hydrogen Energy*, 2020, **45**(3), 1793–1801, DOI: [10.1016/j.ijhydene.2019.11.051](https://doi.org/10.1016/j.ijhydene.2019.11.051).
- 31 C.-J. Chen, K.-C. Yang, C.-W. Liu, Y.-R. Lu, C.-L. Dong, D.-H. Wei, S.-F. Hu and R.-S. Liu, Silicon Microwire Arrays Decorated with Amorphous Heterometal-Doped Molybdenum Sulfide for Water Photoelectrolysis, *Nano Energy*, 2017, **32**, 422–432, DOI: [10.1016/j.nanoen.2016.12.045](https://doi.org/10.1016/j.nanoen.2016.12.045).





- 32 L. Zhang, C. Liu, A. B. Wong, J. Resasco and P. Yang, MoS<sub>2</sub>-Wrapped Silicon Nanowires for Photoelectrochemical Water Reduction, *Nano Res.*, 2015, **8**(1), 281–287, DOI: [10.1007/s12274-014-0673-y](#).
- 33 Z. Huang, C. Wang, L. Pan, F. Tian, X. Zhang and C. Zhang, Enhanced Photoelectrochemical Hydrogen Production Using Silicon Nanowires@MoS<sub>3</sub>, *Nano Energy*, 2013, **2**(6), 1337–1346, DOI: [10.1016/j.nanoen.2013.06.016](#).
- 34 C. Keller, A. Desrues, S. Karuppiiah, E. Martin, J. P. Alper, F. Boismain, C. Villevieille, N. Herlin-Boime, C. Haon and P. Chenevier, Effect of Size and Shape on Electrochemical Performance of Nano-Silicon-Based Lithium Battery, *Nanomaterials*, 2021, **11**(2), 1–15, DOI: [10.3390/nano11020307](#).
- 35 M. Brust, M. Walker, D. Bethell, D. J. Schiffrin and R. Whyman, Synthesis of Thiol-Derivatised Gold Nanoparticles in a Two-Phase Liquid–Liquid System, *J. Chem. Soc. Chem. Commun.*, 1994, **7**, 801–802.
- 36 J. Turkevich, P. C. Stevenson and J. Hillier, A Study of the Nucleation and Growth Processes in the Synthesis of Colloidal Gold, *J. Phys. Chem. Lett.*, 1951, **11**, 55–75, DOI: [10.1039/DF9511100055](#).
- 37 C. Ziegler and A. Eychmuller, Seeded Growth Synthesis of Uniform Gold Nanoparticles with Diameters of 15–300 nm, *J. Phys. Chem. C*, 2011, **115**(11), 4502–4506.
- 38 D. N. Nguyen, M. Fadel, P. Chenevier, V. Artero and P. D. Tran, Water-Splitting Artificial Leaf Based on a Triple-Junction Silicon Solar Cell: One-Step Fabrication through Photoinduced Deposition of Catalysts and Electrochemical Operando Monitoring, *J. Am. Chem. Soc.*, 2022, **144**(22), 9651–9660, DOI: [10.1021/jacs.2c00666](#).
- 39 P. Reiss, M. Carrière, C. Lincheneau, L. Vaure and S. Tamang, Synthesis of Semiconductor Nanocrystals, Focusing on Nontoxic and Earth-Abundant Materials, *Chem. Rev.*, 2016, **116**(18), 10731–10819, DOI: [10.1021/acs.chemrev.6b00116](#).
- 40 U. Langklotz, T. Lein, C. Schulze, M. Weiser, A. Krause and A. Michaelis, Scalable Fabrication of Gold Nanoparticles with Adjustable Size Distribution as Catalytic Nuclei for the CVD Growth of Silicon Nanowires, *Appl. Surf. Sci.*, 2020, **502**, 144203.
- 41 F. Dhalluin, P. J. Desré, M. I. den Hertog, J.-L. Rouvière, P. Ferret, P. Gentile and T. Baron, Critical Condition for Growth of Silicon Nanowires, *J. Appl. Phys.*, 2007, **102**(9), 94906, DOI: [10.1063/1.2811935](#).
- 42 H. Gilman and D. H. Miles, Disproportionation Reaction of Diphenylsilane in the Absence of Any Added Catalyst, *J. Org. Chem.*, 1958, **23**, 326–328, DOI: [10.1021/jo01096a626](#).
- 43 D. C. Lee, T. Hanrath and B. A. Korgel, The Role of Precursor-Decomposition Kinetics in Silicon-Nanowire Synthesis in Organic Solvents, *Angew Chem. Int. Ed. Engl.*, 2005, **44**(23), 3573–3577, DOI: [10.1002/anie.200463001](#).
- 44 H. E. O'Neal, M. A. Ring, D. Kim and K. D. King, Primary Reaction Channels and Kinetics of the Thermal Decomposition of Phenylsilane, *J. Phys. Chem.*, 1995, **99**, 9397–9402.
- 45 M. A. Ring and H. E. O'Neal, Mechanism of the Thermally Induced Gas-Phase Decomposition of Silane: A Revisitation, *J. Phys. Chem.*, 1992, **96**(26), 10848–10855.
- 46 R. E. Jardine, H. E. O'Neal, M. A. Ring and M. E. Beatie, Mechanism of the Thermal Decomposition of Ethylsilane, *J. Phys. Chem.*, 1995, **99**(33), 12507–12511.
- 47 K. L. Walker, R. E. Jardine, M. A. Ring and H. E. O'Neal, Mechanisms and Kinetics of the Thermal Decompositions of Trichlorosilane, Dichlorosilane, and Monochlorosilane, *Int. J. Chem. Kinet.*, 1998, **30**(1), 69–88.
- 48 J. J. Nájera, J. O. Cáceres and S. I. Lane, Gas-Phase Infrared Laser Photolysis of Phenylsilane, *J. Photochem. Photobiol., A*, 2000, **131**(1), 1–11, DOI: [10.1016/S1010-6030\(99\)00215-4](#).
- 49 G. Flynn, K. Stokes and K. M. Ryan, Low Temperature Solution Synthesis of Silicon, Germanium and Si–Ge Axial Heterostructures in Nanorod and Nanowire Form, *Chem. Commun.*, 2018, **54**(45), 5728–5731, DOI: [10.1039/C8CC03075H](#).
- 50 T. Xu, Y. Lambert, C. Krzeminski, B. Grandidier, D. Stiévenard, G. Lévêque, A. Akjouj, Y. Pennec and B. Djafari-Rouhani, Optical Absorption of Silicon Nanowires, *J. Appl. Phys.*, 2012, **112**(3), 033506, DOI: [10.1063/1.4739708](#).
- 51 P. Reiss, M. Carrière, C. Lincheneau, L. Vaure and S. Tamang, Synthesis of Semiconductor Nanocrystals, Focusing on Nontoxic and Earth-Abundant Materials, *Chem. Rev.*, 2016, **116**(18), 10731–10819, DOI: [10.1021/acs.chemrev.6b00116](#).
- 52 J. L. Grosseau-Poussard, P. Moine and J. P. Villain, Microstructural and Tribological Characterization of MoS<sub>x</sub> Coatings Produced by High-Energy Ion-Beam-Assisted Deposition, *Thin Solid Films*, 1993, **224**(1), 52–57, DOI: [10.1016/0040-6090\(93\)90457-Z](#).
- 53 P. D. Tran, M. Nguyen, S. S. Pramana, A. Bhattacharjee, S. Y. Chiam, J. Fize, M. J. Field, V. Artero, L. H. Wong, J. Loo and J. Barber, Copper Molybdenum Sulfide: A New Efficient Electrocatalyst for Hydrogen Production from Water, *Energy Environ. Sci.*, 2012, **5**(10), 8912, DOI: [10.1039/c2ee22611a](#).
- 54 Y. Wang, K.-K. Lew, T.-T. Ho, L. Pan, S. W. Novak, E. C. Dickey, J. M. Redwing and T. S. Mayer, Use of Phosphine as an N-Type Dopant Source for Vapor–Liquid–Solid Growth of Silicon Nanowires, *Nano Lett.*, 2005, **5**(11), 2139–2143, DOI: [10.1021/nl051442h](#).
- 55 M. Legallais, T. T. Nguyen, M. Mouis, B. Salem, E. Robin, P. Chenevier and C. TERNON, An Innovative Large Scale Integration of Silicon Nanowire-Based Field Effect Transistors, *Solid State Electron.*, 2018, **143**, 97–102, DOI: [10.1016/j.sse.2017.11.008](#).
- 56 S. Chandrasekaran, N. Kaeffer, L. Cagnon, D. Aldakov, J. Fize, G. Nonglaton, F. Baleras, P. Mailley and V. Artero, A Robust ALD-Protected Silicon-Based Hybrid Photoelectrode for Hydrogen Evolution under Aqueous Conditions, *Chem. Sci.*, 2019, **10**(16), 4469–4475, DOI: [10.1039/C8SC05006F](#).
- 57 D. G. Boucher, K. Kearney, E. Ertekin and M. J. Rose, Tuning P-Si(111) Photovoltage via Molecule|Semiconductor



- Electronic Coupling, *J. Am. Chem. Soc.*, 2021, **143**(6), 2567–2580, DOI: [10.1021/jacs.0c12075](https://doi.org/10.1021/jacs.0c12075).
- 58 B. Wu, T. Wang, B. Liu, H. Li, Y. Wang, S. Wang, L. Zhang, S. Jiang, C. Pei and J. Gong, Stable Solar Water Splitting with Wettable Organic-Layer-Protected Silicon Photocathodes, *Nat. Commun.*, 2022, **13**(1), 4460, DOI: [10.1038/s41467-022-32099-1](https://doi.org/10.1038/s41467-022-32099-1).
- 59 P. Gentile, T. David, F. Dhalluin, D. Buttard, N. Pauc, M. D. Hertog, P. Ferret and T. Baron, The Growth of Small Diameter Silicon Nanowires to Nanotrees, *Nanotechnology*, 2008, **19**(12), 125608, DOI: [10.1088/0957-4484/19/12/125608](https://doi.org/10.1088/0957-4484/19/12/125608).
- 60 A. B. Laursen, P. C. K. Vesborg and I. Chorkendorff, A High-Porosity Carbon Molybdenum Sulphide Composite with Enhanced Electrochemical Hydrogen Evolution and Stability, *Chem. Commun.*, 2013, **49**(43), 4965–4967, DOI: [10.1039/C3CC41945B](https://doi.org/10.1039/C3CC41945B).
- 61 L. Zhang, L. Wu, J. Li and J. Lei, Electrodeposition of Amorphous Molybdenum Sulfide Thin Film for Electrochemical Hydrogen Evolution Reaction, *BMC Chem.*, 2019, **13**(1), 88, DOI: [10.1186/s13065-019-0600-0](https://doi.org/10.1186/s13065-019-0600-0).
- 62 G. Zeng, T. A. Pham, S. Vanka, G. Liu, C. Song, J. K. Cooper, Z. Mi, T. Ogitsu and F. M. Toma, Development of a Photoelectrochemically Self-Improving Si/GaN Photocathode for Efficient and Durable H<sub>2</sub> Production, *Nat. Mater.*, 2021, **20**(8), 1130–1135, DOI: [10.1038/s41563-021-00965-w](https://doi.org/10.1038/s41563-021-00965-w).
- 63 A. Morozan, H. Johnson, C. Roiron, G. Genay, D. Aldakov, A. Ghedjatti, C. T. Nguyen, P. D. Tran, S. Kinge and V. Artero, Nonprecious Bimetallic Iron-Molybdenum Sulfide Electrocatalysts for the Hydrogen Evolution Reaction in Proton Exchange Membrane Electrolyzers, *ACS Catal.*, 2020, 14336–14348, DOI: [10.1021/acscatal.0c03692](https://doi.org/10.1021/acscatal.0c03692).

